AIAA Journal
Vol. 45, No. 11, November 2007

In Situ Imaging of Crack Growth with Piezoelectric-Wafer Active Sensors

Victor Giurgiutiu[*] and Lingyu Yu[†]
University of South Carolina, Columbia, South Carolina 29208
James R. Kendall III[‡]
Lockheed Martin Space Systems Company, New Orleans, Louisiana 70129
and
Christopher Jenkins[§]
TRANE Corporation, Columbia, South Carolina 29169

DOI: 10.2514/1.30798

Piezoelectric-wafer active sensors are small, inexpensive, noninvasive, elastic wave transmitters/receivers that can be easily affixed to a structure. As wide-band nonresonant devices, piezoelectric-wafer active sensors can selectively tune in various Lamb-wave modes traveling in a thin-wall structure. This paper presents results obtained using a linear piezoelectric-wafer phased array to in situ image crack growth during a simulated structural health monitoring test on a large 2024-T3 aluminum plate. During the test, in situ readings of the piezoelectric-wafer phased array were taken in a round-robin fashion while the testing machine was running. Additional hardware was incorporated to prefilter the received signals before digitization to obtain usable readings. The received signals were postprocessed with the embedded ultrasonic structural radar phased-array algorithm and a direct imaging of the crack in the test plate was obtained. The imaging results were compared with physical measurements of the crack size using a digital camera. Good consistency was observed. The results of this investigation could be used to predict the gradual growth of a crack during structural health monitoring.

Nomenclature

a = half-length of the piezoelectric-wafer transducer; also, crack length
c = wave speed
D_j = electrical displacement
d_{kij} = piezoelectric coupling
E_k = electrical field
$F_{\min}$ = minimum load
$F_{\max}$ = maximum load
i = imaginary constant $i = \sqrt{-1}$
i, j = indices
J_1, H_1 = Bessel functions
K = stress-intensity factor
K_c = critical stress-intensity factor
p_{ij} = elemental signals
R = ratio of minimum to maximum load $R = F_{\min}/F_{\max}$
r = radial location
r_Y = crack-tip plastic zone radius
S^E_{ijkl} = mechanical compliance of the material measured at zero electric field, $E = 0$
S_{ij} = mechanical strain
T_{kl} = mechanical stress
Y = yield stress
α, β = wave numbers
δ_i, δ_j = delays used in phased-array calculations
ε^T_{jk} = dielectric permittivity measured at zero mechanical stress, $T = 0$
ε_x = strain in the x direction
μ = shear modulus of the material (equivalent to the engineering constant G)
ξ = wave number
σ = stress
τ_0 = shear stress at the interface between piezoelectric wafer and structure
ϕ_0 = steering angle
ω = circular frequency, rad/s

Superscripts

S = symmetric modes
A = antisymmetric modes

I. Introduction

STRUCTURAL health monitoring (SHM) is an emerging technology that is posed to transition the conventional ultrasonic nondestructive evaluation (NDE) methods to embedded systems that will be capable of performing on-demand interrogation of structural health. SHM requires the development of small, lightweight, inexpensive, unobtrusive, minimally invasive sensors to be embedded in the airframe with minimum weight penalty and at affordable costs. Such sensors should be able to scan the structure and identify the presence of defects and incipient damage. Current ultrasonic inspection of thin-wall structures (e.g., aircraft shells, storage tanks, large pipes, etc.) is a time-consuming operation which requires meticulous through-the-thickness C-scans over large areas. One method to increase the efficiency of thin-wall structures inspection is to use guided waves (e.g., Lamb waves) instead of the conventional pressure waves. Guided waves propagate along the midsurface of thin-wall plates and shallow shells. They can travel relatively large distances with very little amplitude loss and offer the advantage of large-area coverage with a minimum of installed

---

Presented as Paper 2114 at the 47th AIAA/ASME/ASCE/AHS/ASC Structures, Structural Dynamics & Materials Conference and 14th AIAA/ASME/AHS Adaptive Structures Conference, Newport, RI, 1–5 May 2006; received 3 March 2007; revision received 4 June 2007; accepted for publication 5 June 2007. Copyright © 2007 by Victor Giurgiutiu. Published by the American Institute of Aeronautics and Astronautics, Inc., with permission. Copies of this paper may be made for personal or internal use, on condition that the copier pay the $10.00 per-copy fee to the Copyright Clearance Center, Inc., 222 Rosewood Drive, Danvers, MA 01923; include the code 0001-1452/07 $10.00 in correspondence with the CCC.

[*] Professor of Mechanical Engineering, Department of Mechanical Engineering; victorg@sc.edu. Senior Member AIAA.

[†] Postdoctoral Research Associate, Department of Mechanical Engineering; yu3@engr.sc.edu.

[‡] Quality Assurance Engineer; James.R.Kendall@maf.nasa.gov.

[§] Applications Specialist; cjenkins@trane.com.

sensors. Guided Lamb waves have opened new opportunities for cost-effective detection of damage in aircraft structures, and a large number of papers have recently been published on this subject. Traditionally, guided waves have been generated by impinging the plate obliquely with a tone-burst from a relatively large ultrasonic transducer. However, conventional Lamb-wave probes (wedge and comb transducers) are relatively too heavy and expensive to consider for widespread deployment on an aircraft structure as part of an SHM system. Hence, a different type of sensor than the conventional ultrasonic transducers is required for the SHM systems. One way of addressing this need is through the piezoelectric-wafer active sensors (PWAS), which are lightweight and inexpensive transducers that can act as both transmitters and receivers of guided waves in thin-wall structures [1–9].

In this paper, we will demonstrate the technique of using PWAS transducers to detect crack growth in a thin-wall specimen through a direct-imaging technique, the embedded ultrasonic structural radar (EUSR) PWAS phased-array algorithm. Here ultrasonic guided waves (Lamb waves) transmitted and received with PWAS transducers will be used in conjunction with the phased-array principle to image a thin-plate specimen being fatigued in a testing machine. The crack growth is directly measured from the EUSR image and compared with optical photos taken with a digital camera.

After a short review of the PWAS transducer principles, the paper will explain PWAS interaction with the guided Lamb waves in the structure, and their capability to selectively tune into specific Lamb-wave modes. Then we will show how to apply the tuned Lamb-wave modes (in particular, the low-dispersion S0 mode) in conjunction with the phased-array theory to scan and image a thin-wall specimen under monitoring. In our particular application, data are collected in a round-robin fashion, i.e., one PWAS at a time serves as transmitter while others receive, and all PWAS serve as the transmitter in turn. Then the phased-array principle is applied to the collected data in virtual time as a signal postprocessing procedure. The paper continues with a brief recall of the linear elastic fracture mechanics principles used in the design of the experimental specimen. The aim of this specimen design is to create the conditions under which sizable crack growth can be generated in a plate specimen during a reasonable testing period. Low-cycle fatigue principles, combined with fracture mechanics crack-growth theory used in the specimen design are reviewed. After all these theoretical preliminaries, the paper next presents the experimental setup used during the tests. Data collection is carried out during actual fatigue testing; thus signal filtering and noise rejection is critical for extracting useful signals from the significant noise caused by the cycling testing and adjacent vibrations. Experimental procedure consists of two steps: 1) validation of the crack-growth assumptions, which will be done on a plain specimen without PWAS instrumentation; and 2) validation of the PWAS EUSR imaging of crack growth, which will be done on a fully instrumented second specimen. Discussion of the experimental results indicates that the crack-growth direct imaging using ultrasonic guided waves in situ PWAS phased array compares very well with the photos taken with a digital optical camera. Limitation of the present method is also discussed, mostly due to the size of the PWAS phased-array aperture, distance from the crack to the array, and crack orientation with respect to the array. Suggestions for further work are given at the end of the paper.

II. Guided-Wave Generation/Detection with PWAS Transducers

In recent years, piezoelectric wafers permanently attached to the structure have been used for the guided waves generation and detection. We have named these devices piezoelectric-wafer active sensors [1]. PWAS are inexpensive, nonintrusive, unobtrusive devices that can be used in both active and passive modes. In the active mode, PWAS generated Lamb waves can be used for damage detection through pulse-echo, pitch-catch, phased-array, or electromechanical (E/M) impedance techniques. In the passive mode, PWAS can act as receivers of Lamb waves generated by low-velocity impacts or by acoustic emission at propagating crack tips.

PWAS operate on the piezoelectric principle that couples the electrical and mechanical variables in the material (mechanical strain S_{ij}, mechanical stress T_{kl}, electrical field E_k, and electrical displacement D_j) in the form

$$S_{ij} = s^E_{ijkl} T_{kl} + d_{kij} E_k \qquad D_j = d_{jkl} T_{kl} + \varepsilon^T_{jk} E_k \tag{1}$$

where S^E_{ijkl} is the mechanical compliance of the material measured at zero electric field ($E = 0$), ε^T_{jk} is the dielectric permittivity measured at zero mechanical stress ($T = 0$), and d_{kij} represents the piezoelectric coupling effect. For embedded NDE applications, PWAS couple their in-plane motion, excited by the applied oscillatory voltage through the piezoelectric effect, with the Lamb-waves particle motion on the material surface. Lamb waves can be either quasi axial (S0, S1, S2, ...) or quasi flexural (A0, A1, A2, ...). Figure 1 shows the interaction between surface-mounted PWAS and S0- and A0-guided Lamb waves.

The in-plane interaction between the PWAS and the guided Lamb waves is such that preferential tuning can be achieved when the representative PWAS dimensions are near an odd multiple of the half-wavelength of certain Lamb-wave modes. Thus, selective tuning of various Lamb-wave modes can be achieved by setting the PWAS dimension to be the appropriate multiple of the half-wavelength [10]. Giurgiutiu and Lyshevski [10] developed the theory of the interaction of a rectangular PWAS with one-dimensional propagation, i.e., straight-crested Lamb waves, and presented tuning prediction formulas based on trigonometric functions.

$$\varepsilon_x(x,t)|_{y=d} = -i\frac{a\tau_0}{\mu}\left[\sum_{\xi^S}\sin(\xi^S a)\frac{N_S(\xi^S)}{D'_S(\xi^S)}e^{i(\xi^S x-\omega t)} + \sum_{\xi^A}\sin(\xi^A a)\frac{N_A(\xi^A)}{D'_A(\xi^A)}e^{i(\xi^A x-\omega t)}\right] \tag{2}$$

where

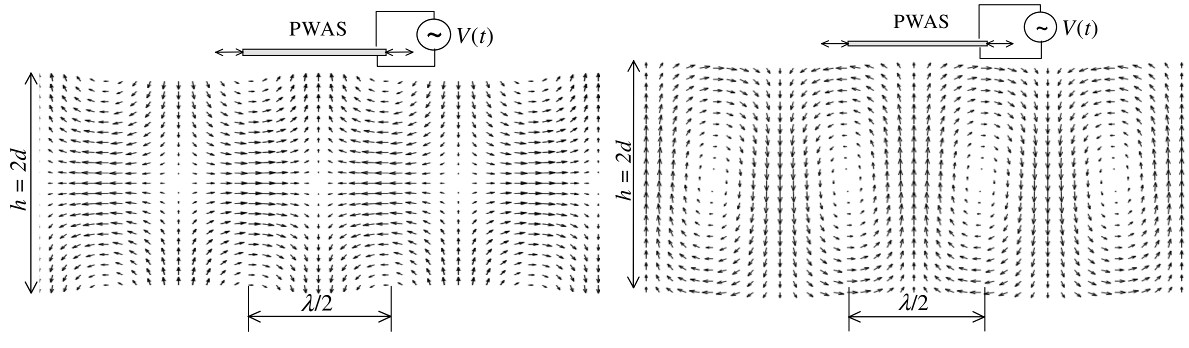

a) S0 mode **b) A0 mode**

Fig. 1 PWAS interaction with Lamb waves in a plate at applied alternating voltage $V(t)$. Plate thickness is h, $h = 2d$ where d is half-plate thickness.

$$N_S = \xi\beta(\xi^2 + \beta^2)\cos(\alpha d)\cos(\beta d)$$
$$N_A = \xi\beta(\xi^2 + \beta^2)\sin(\alpha d)\sin(\beta d)$$
$$D_S = (\xi^2 - \beta^2)^2\cos(\alpha d)\sin(\beta d) + 4\xi^2\alpha\beta\sin(\alpha d)\cos(\beta d)$$
$$D_A = (\xi^2 - \beta^2)^2\sin(\alpha d)\cos(\beta d) + 4\xi^2\alpha\beta\cos(\alpha d)\sin(\beta d)$$

where ξ^S and ξ^A are the zeros of D_S and D_A, respectively. We can note that these are the solutions of the Rayleigh–Lamb equation. Raghavan and Cesnik [11] extended these results to the case of a circular transducer coupled with circular-crested Lamb waves and proposed corresponding tuning prediction formulas based on Bessel functions:

$$\varepsilon_r(r,t)|_{z=d} = \pi\frac{\tau_0 a}{\mu}e^{i\omega t}\left[\sum_{\xi^S} J_1(\xi^S a)\xi^S\frac{N_S(\xi^S)}{D'_S(\xi^S)}H_1^{(2)}(\xi^S r) + \sum_{\xi_A} J_1(\xi^A a)\xi^A\frac{N_A(\xi^A)}{D'_A(\xi^A)}H_1^{(2)}(\xi^A r)\right] \tag{3}$$

A comprehensive study of these prediction formulas in comparison experimental results has recently been performed by Bottai and Giurgiutiu [12]. Experiments were performed on large aluminum alloy plates using square, circular, and rectangular PWAS. Frequencies up to 700 kHz were explored. Two plate thicknesses were studied, 1.07 and 3.15 mm. In the thinner plate, only two Lamb-wave modes, A0 and S0, were present in the explored frequency range. In the thicker plate, a third Lamb wave, A1, was also present. Figure 2 gives the results for a 7 mm square PWAS placed on 1.07 mm 2024-T3 aluminum alloy plate.

The experimental results (Fig. 2a) show that a rejection of the highly dispersive A0 Lamb-wave mode is observed at around 200 kHz. At this frequency, only the S0 mode is excited, which is very beneficial for pulse-echo studies due to the low-dispersion of the S0 mode at this relatively low value of the fd product. On the other hand, a strong excitation of the A0 mode is observed at around 50 kHz. These experimental results were reproduced using Eq. (2) with the assumption that the effective PWAS length is 6.4 mm (Fig. 2b, [12]). The difference between the actual PWAS length and effective PWAS length is attributed to shear transfer/diffusion effects at the PWAS boundary.

III. Direct Structural Imaging with EUSR-PWAS Phased Arrays

By using Lamb waves in a thin-wall structure, one can detect the existence and positions of cracks, corrosions, delaminations, and other damage [13,14]. PWAS transducers act as both transmitters and receivers of Lamb waves traveling in the plate. Upon excitation with an electric signal, the PWAS generate Lamb waves into a thin-wall structure. The generated Lamb waves travel into the structure and are reflected or diffracted by the structural boundaries, discontinuities, and damage. The reflected or diffracted waves arrive back at the PWAS where they are transformed into electric signals.

Of particular interest is the phased-array implementation of this concept. The embedded ultrasonic structural radar is a phased-array application of the PWAS technology. The EUSR principles and initial results were reported extensively by Giurgiutiu and Bao [15] and an improved implementation algorithm was updated by Yu and Giurgiutiu [16]. The basic idea is to use a group of PWAS arranged in a certain pattern and manipulate the synthetic output beam at a particular direction by adjusting the delays between the firing of each element. Among the possible array configurations, the linear array obtained by arranging elements along a straight line presents as the simplest one, as illustrated in Fig. 3. A 4 ft^2 aluminum plate is instrumented with an M-PWAS linear array ($M = 8$ in this particular application). The PWAS array will be used to image the upper half of the plate and to detect structural damage through the EUSR algorithm. The HP33120 signal generator will be used to send out the excitation signal, and reception signals will be collected by the TDS210 digital oscilloscope. Switching between transmission and reception will be implemented through the automated signal collection unit (ASCU) system [17]. The damage shown here is simulated by a 20 mm narrow slit as a through-the-thickness crack, arranged at 90 deg to the array. After tuning, the excitation frequency was determined to be 282 kHz, a frequency at which essentially only the S0 mode is excited.

To simplify the instrumentation requirement, data collection was conducted in a round-robin pattern, resulting a $M \times M$ matrix of elemental signals $[p_{ij}(t)]$ as shown in Table 1.

The round-robin pattern excites one PWAS at a time and receives on all the other PWAS; all PWAS serve as the transmitter in turn. After the total of M^2 signals are collected and stored in the computer memory, the phased-array beamforming is implemented in virtual time using the EUSR algorithm [16] based on the delay-and-sum phased-array principle such that

$$s_R(t;\phi_0) = \sum_{i=0}^{M-1}\sum_{j=1}^{M-1} p_{ij}[t - \delta_i(\phi_0) - \delta_j(\phi_0)] \tag{4}$$

where ϕ_0 is the steering direction and $\delta_i(\phi_0)$, $\delta_j(\phi_0)$ are delays applied to the corresponding PWAS. It is noticed that delays depend on both the PWAS elementary parameters and the direction ϕ_0. For the target located at point $P(r,\phi_0)$, the delay applied to the mth element is

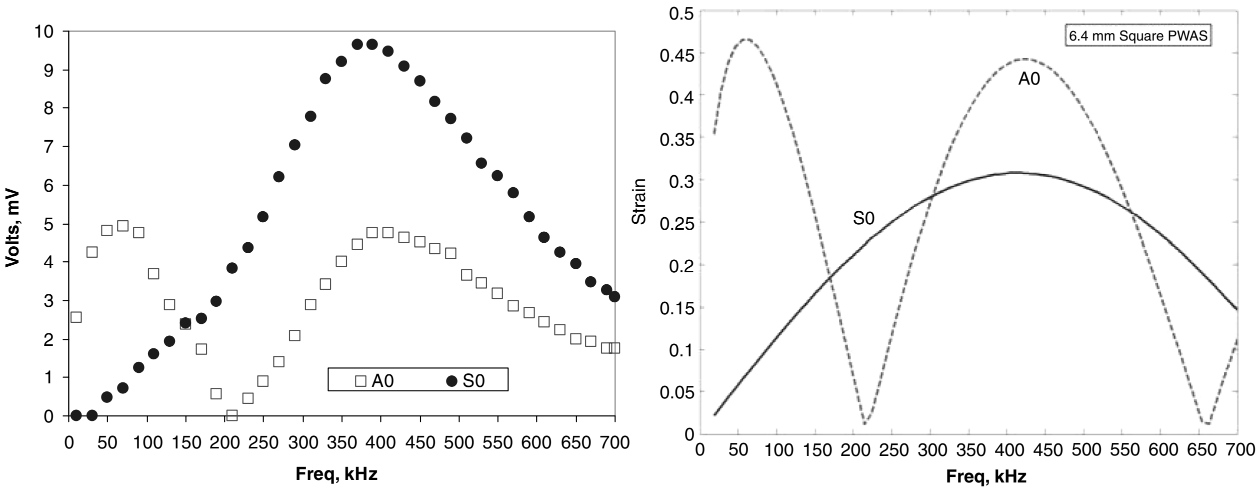

a) Experimental results

b) Prediction with Eq. (2)

Fig. 2 Lamb-wave tuning using a 7 mm square PWAS placed on 1.07 mm 2024-T3 aluminum alloy plate.

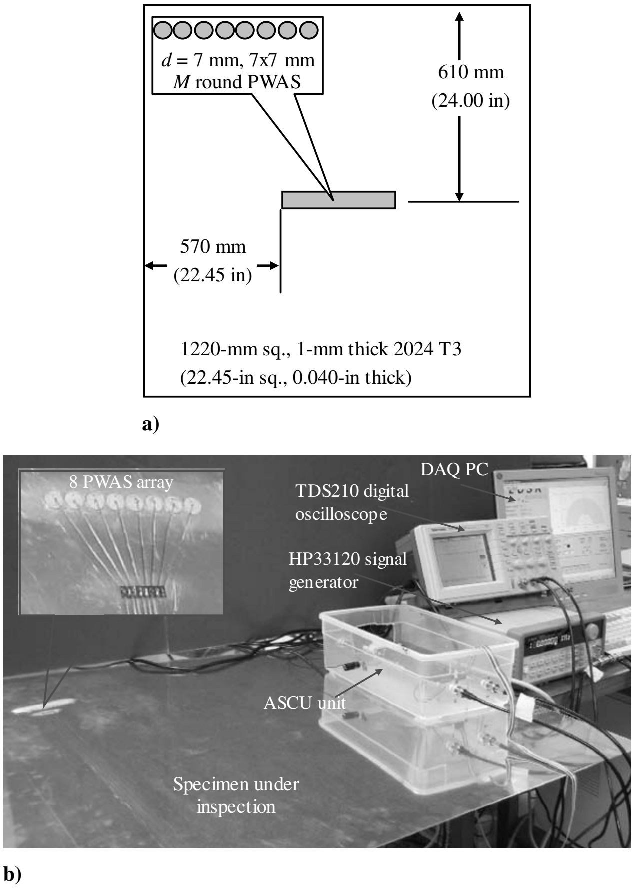

Fig. 3 Laboratory crack detection experiment using an eight-PWAS linear phased array: a) specimen schematic, b) experimental equipment setup.

$$\delta_m(\phi_0) = \frac{r - r_m}{c} \tag{5}$$

where r_m is the distance from PWAS element to the target P and c is the wave-propagation speed.

A LabVIEW program was constructed to implement the EUSR algorithm and the associated signal processing, as described in [16]. The elemental signals of Table 1 are processed using the phased-array beamforming formulas as a function of a variable azimuthal angle ϕ_0, which is allowed to vary in the range 0–180 deg. Note that the scanning range is limited to 0–180 deg because the resulting beam is symmetric with respect to the axis of the elements in the linear array. Thus a sweep of the complete half-plane is attained. At each azimuthal angle, an A-scan of the Lamb-wave beam signal is also obtained. When such a beam encounters damage, reflection/diffraction from the damage will show as an echo. Azimuthal juxtaposition of all the A-scan signals creates an image of the half-plane. A scanning image of the specimen (Fig. 3) is provided in Fig. 4. The damage is clearly indicated as darker areas. Using the group velocity value of 5.44 mm/μs at the designated excitation frequency (282 kHz), the time-domain signals are mapped into the space domain. A measuring grid is superposed on the reconstructed image to find the geometric position of the damage. Thus the exact location of the damage can be directly determined. Meanwhile, the A-scan extracted at 90 deg clearly indicates the crack echo.

The EUSR steering beam method based on PWAS phased arrays has been verified by detecting various structural defects [18]. Figure 5 shows the simultaneous detection of two cracks, which were placed symmetrically offside the PWAS phased array. Here offside refers to any direction but 90 deg with respect to the axis of the linear array. Another concern was related to the probability of detection (POD) with this method. In an initial investigation, experiments were conducted to determine the smallest damage that the EUSR method could detect [18]. It was found that a through hole with a diameter as small as 1.57 mm can be detected by EUSR imaging (Fig. 6). However, though the sensitivity of EUSR is confirmed, further investigation is needed to improve the resolution such that the difference between a small hole and a small crack can be detected.

IV. Review of Linear Elastic Fracture Mechanics Principles

A. Stress-Intensity Factor

The stress-intensity factor at a crack tip has the general expression

$$K(\sigma, a) = C\sigma\sqrt{\pi a} \tag{6}$$

where σ is the applied stress, a is the crack length, and C is a constant depending on the specimen geometry and loading distribution [19]. Note that the stress-intensity factor increases not only with the applied stress σ, but also with the crack length a. If the crack length is too long, a critical state is achieved when the crack growth becomes rapid and uncontrollable. The value of K associated with rapid crack extension is called the critical stress-intensity factor K_c. For a given material, the onset of rapid crack extension occurs always at the same stress-intensity value K_c. For different specimens, having different initial crack lengths and geometries, the stress level σ, at which rapid crack extension occurs, may be different. However, the K_c value will always be the same. Therefore, K_c can serve as a property of the material. Thus the condition for fracture to occur is that the local stress-intensity factor $K(\sigma, a)$ exceeds the value K_c, i.e.,

$$K(\sigma, a) \geq K_c \tag{7}$$

We see that K_c provides a single-parameter fracture criterion that allows the prediction of fracture. Although the detailed calculation of $K(\sigma, a)$ and determination of K_c may be difficult in some cases, the general concept of using K_c to predict brittle fracture remains nonetheless applicable. The K_c concept can be also extended to materials that posses some limited ductility, such as high-strength metals. In this case, the $K(\sigma, a)$ expression (6) is modified to account for a crack-tip plastic zone r_Y, such that

$$K(\sigma, a) = C\sigma\sqrt{\pi(a + r_Y)} \tag{8}$$

where the maximum value of r_Y can be estimated as

$$r_{Y\sigma} = \frac{1}{2\pi}\sqrt{\frac{K_c}{Y}} \tag{9}$$

Table 1 $M \times M$ matrix of elemental signals generated in a round-robin in the PWAS phase-array [1]

		Firing pattern (symbol T_j designates the transmitter that is activated)				
		T_0	T_1	T_2	——	T_{M-1}
Receivers	R_0	$p_{0,0}(t)$	$p_{0,1}(t)$	$p_{0,2}(t)$	——	$p_{0,M}(t)$
	R_1	$p_{1,0}(t)$	$p_{1,1}(t)$	$p_{1,2}(t)$	——	$p_{1,M}(t)$
	R_2	$p_{2,0}(t)$	$p_{2,1}(t)$	$p_{2,2}(t)$	——	$p_{2,M}(t)$
	——	——	——	——	——	——
	R_{M-1}	$p_{M-1,0}(t)$	$p_{M-1,1}(t)$	$p_{M-1,2}(t)$	——	$p_{M-1,M-1}(t)$

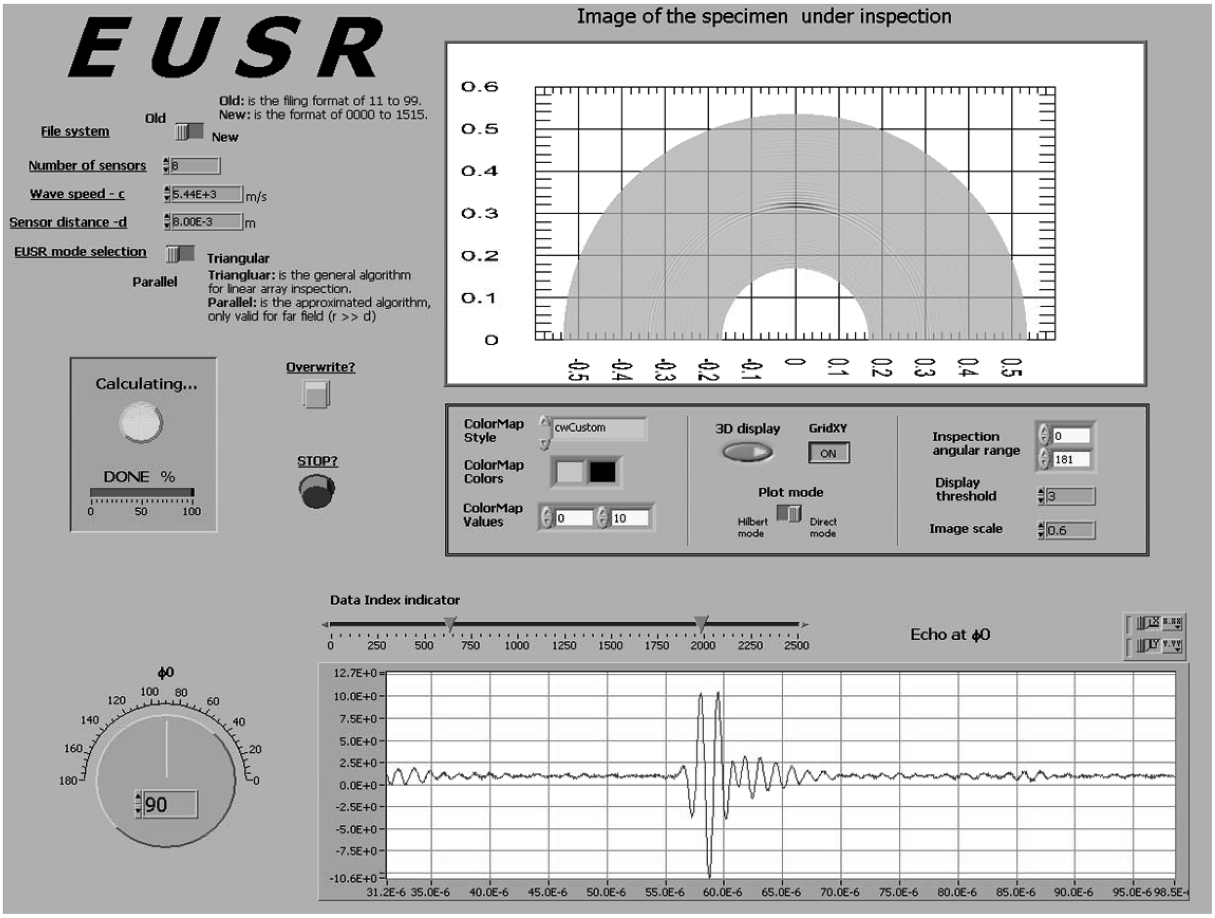

Old: is the filing format of 11 to 99.
New: is the format of 0000 to 1515.

File system: Old / New

Number of sensors: 8

Wave speed - c: 5.44E+3 m/s

Sensor distance -d: 8.00E-3 m

EUSR mode selection: Triangular / Parallel

Triangluar: is the general algorithm for linear array inspection.
Parallel: is the approximated algorithm, only valid for far field (r >> d)

ColorMap Style: cwCustom

ColorMap Colors

ColorMap Values: 0 10

Inspection angular range: 0 181

Display threshold: 3

Image scale: 0.6

ϕ0: 90

Fig. 4 Specimen scanning image and A-scan at 90 deg with crack echo as displayed in the EUSR GUI front panel.

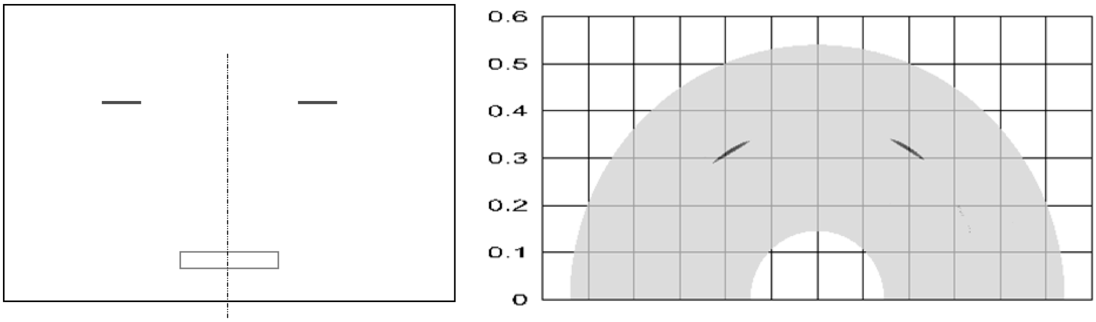

a) Specimen schematic **b) EUSR scanning image [18]**

Fig. 5 EUSR detection of two cracks symmetrically placed offside of the PWAS phased array, at 67 and 117 deg, respectively.

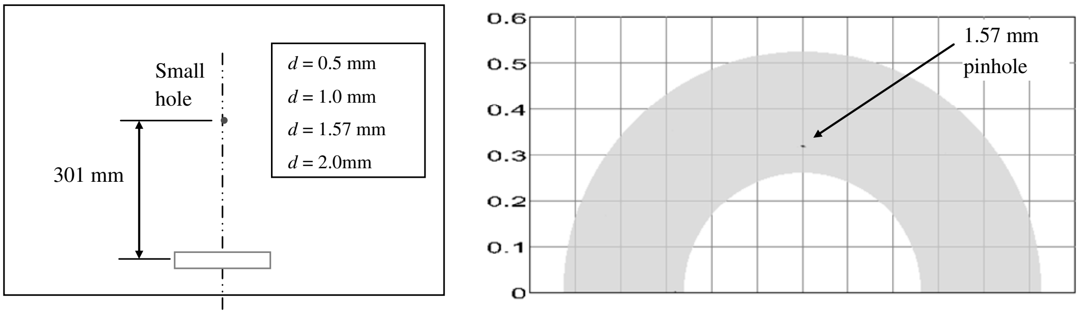

a) Specimen schematic **b) EUSR scanning image of min detectable pinhole [18]**

Fig. 6 EUSR detection of broadside pinholes about 301 mm from the array (diameter of the hole changes from 0.5 to 1, 1.57, and 2 mm).

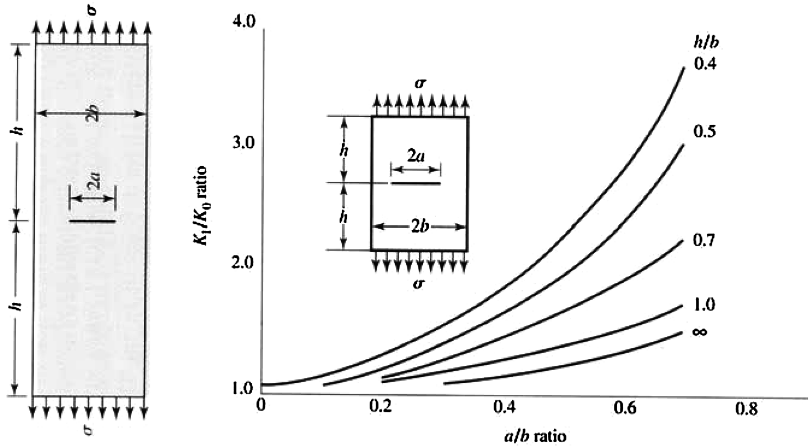

Fig. 7 Plate containing a central crack length of 2*a*. Tensile stress σ acts in the longitudinal direction [25].

for plane stress, and

$$r_{Y\sigma} = \frac{1}{6\pi}\sqrt{\frac{K_c}{Y}} \tag{10}$$

for plane strain. In studying the material behavior, one finds that the plane-strain conditions give the lowest value of K_c, whereas the plane-stress conditions can give K_c values that may be from 2 to 10 times higher. This effect is connected with the degree of constraint imposed upon the material. The materials with higher constraint effects have a lower K_c value. The plain-strain condition is the condition with most constraint. The plain-strain K_c is also called the fracture toughness K_{Ic} of the material. Standard test methods exist for determining the material fracture toughness value. When used in design, the fracture toughness criteria gives a larger margin of safety than elastic-plastic fracture mechanics methods such as 1) crack opening displacement (COD) methods, 2) R-curve methods, or 3) J-integral methods. However, the fracture toughness approach is more conservative: it is safer, but results in heavier designs. For a complete design analysis, the designer should consider, in most cases, both conditions: 1) the possibility of failure by brittle fracture, and 2) the possibility of failure by ductile yielding. The concepts of linear fracture mechanics can be found in detail in [20–24].

B. Design of the Experimental Specimen

For the proposed experiment, we considered a rectangular specimen with a crack in the middle. For such a specimen, the equation for the stress intensity for mode 1 testing is

$$K_I = \beta\sigma\sqrt{\pi a} \tag{11}$$

where σ is the applied tensile stress, a is half of the crack length, and $\beta = K_I/K_0$. The value of the parameter β (Fig. 7) has been determined numerically for a large variety of specimen geometries and can be found in the literature [25].

The experimental specimen is a 1 mm thick 2024-T3 aluminum plate with the dimensions 600 × 700 mm (24 × 28 in.). The specimen is loaded through a preexisting loading jig that has 17 16 mm holes on two rows with 50 mm pitch and 38 mm row spacing (Fig. 8). The presence of the loading holes imposes special requirements on the specimen design. (Because the loading jig already existed in the lab, the specimen design had to be adapted to the existing loading holes.) The loading holes weakened the specimen. Two strength concerns and one fracture concern had to be simultaneously considered with respect to the specimen loading holes: 1) the bearing strength of the hole, 2) the shearing strength of the "plugs" between the holes and the sides of the specimen, and 3) the stress concentration at the holes should not promote fatigue cracking. In assessing these concerns, standard aircraft design practice guidelines for sheet-metal joints were used [26].

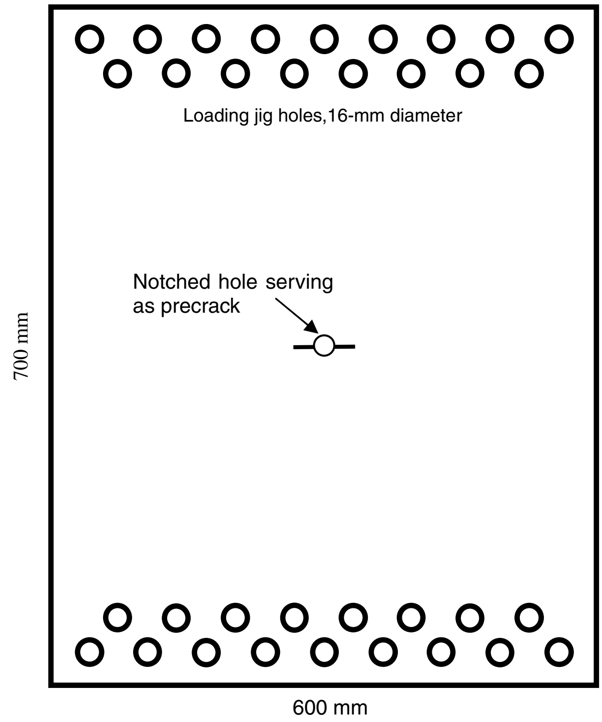

Fig. 8 Schematic of specimen plate no. 1 for assessing the crack-growth rate parameters.

The cyclic fatigue load was considered varying between an upper value $F_{\max}$ and a lower value $F_{\min}$. Because the specimen was of thin sheet-metal construction susceptible to buckling under compression, only tensile loads were considered. An R-ratio of 0.1 was selected ($R = F_{\min}/F_{\max}$). Thus the alternate part of the cyclic loading was $F_a = 0.45F_{\max}$, whereas the mean part of the cyclic loading was $F_m = 0.55F_{\max}$. The strength concerns 1 and 2 were considered to be affected only by $F_{\max}$, whereas the stress concentration and crack propagation, concern 3, was affected by both F_a and F_m. We concluded that a cyclic load of the specimen that would be safe for the bearing holes would be in the range $F_{\max} = 30,000$ kN, $R = 0.1$. The length of the precrack made into the specimen center had to be calculated such that the applied cyclic load would promote crack propagation from the precrack. The cyclic load determined to be safe for the bearing holes was used to calculate the minimum precrack length that would promote crack propagation in the specimen. After performing the analysis, it was determined that an initial precrack length $2a = 50$ mm would be sufficient to achieve a crack-intensity factor $\Delta K = 7.5\ \mathrm{MPa}\sqrt{\mathrm{m}}$ that will ensure an initial crack propagation at a comfortable rate according to Paris' law [21].

V. Experimental Results

The experiments were conducted in two stages. In the first stage, experiments were aimed at determining the initial crack length and the loading conditions that will ensure crack nucleation and a controllable crack growth. In the second stage, the experiments were aimed at actually verifying that the crack growth can be directly imaged with the in situ PWAS phased array using the EUSR algorithm. In addition, the first-stage experiments provided the crack-growth parameters used in the second-stage experiments.

A. Stage 1 Experiments: Fatigue Testing Without PWAS

The stage 1 experiments were performed on specimen no. 1, without PWAS transducers. A notched hole was machined in the middle of the specimen. The diameter of the hole was 6.4 mm (one-quarter inch) and the total precrack length was 53.8 mm (2.12 in.). The specimen was placed in an MTS 810 testing machine, as shown in Fig. 9a. Cyclic loading was applied with $F_{\max} = 17,800$ N (4000 lbf), $F_{\min} = 1780$ N (400 lbf), and $R = 0.1$. A total of 350 kcycles were applied at a frequency of 10 Hz. The crack length was measured every 20 kcycles using a microscope attached to a digital caliper. The crack-growth results are shown in Fig. 10, indicating that the crack-growth behavior resembles Paris' law. It is significant to note that the crack growth started to accelerate after 300 kcycles, which is consistent with Paris' law as well. At the end of the experiment, the crack had grown from the initial 54 mm to approximately 210 mm. The corresponding stress-intensity factors were $K_{\text{initial}} \cong 7.5\ \text{MPa}\sqrt{\text{m}}$ and $K_{\text{final}} \cong 15.3\ \text{MPa}\sqrt{\text{m}}$.

B. Stage 2 Experiments: Fatigue Test with PWAS

The specimen for fatigue testing with PWAS transducers was numbered no. 2. The specimen construction is similar to that of specimen no. 1 used for fatigue testing without PWAS, except

1) The precrack was moved from the center to one side of the specimen, approximately 180 mm north of center (Fig. 11a).

2) A 10-element PWAS array was placed in the center of the specimen (Fig. 11a).

The precrack was 125 μm wide and 30 mm long. The linear PWAS array consisted of 10 1 mm^2 PWAS, 200 μm in thickness and with electrodes on both sides. To minimize the reflections from the loading holes and the plate boundary, a "clay frame" was placed around the PWAS and crack area (Fig. 12).

Instrumentation setup is shown in Fig. 11b. It consisted of an HP 33120 signal generator, a TDS210 digital oscilloscope, an ASCU autoswitch unit, and a laptop computer. The round-robin data collection was performed in the following way: a three-count 372 kHz tone-burst excitation signal was synthesized in the function generator. At this frequency, the tone-burst signal obtained the optimum tuning of the PWAS with the S0 Lamb-wave mode being excited. The tone-burst signal is sent to one PWAS in the array, travels into the plate, and is reflected at the plate boundary. The reflected Lamb-waves packet is received back at the PWAS array. The signals received at each PWAS in the array (including the transmitting PWAS) are collected by a digital acquisition device, i.e., a digital oscilloscope. This procedure generates a column of 10 elemental signals in the 100 elemental-signals array. After this, the cycle is repeated for the other PWAS in the round-robin fashion. For the 10-PWAS array, there will be 10 such measurement cycles necessary to complete the whole data collection process.

1. *Part 1: Validation of the Experimental Method with PWAS*

The first task in our experiment on fatigue with PWAS was to validate our experimental method. Two issues need to be proved:

1) Determine if usable signals could be collected during the fatigue cycling.

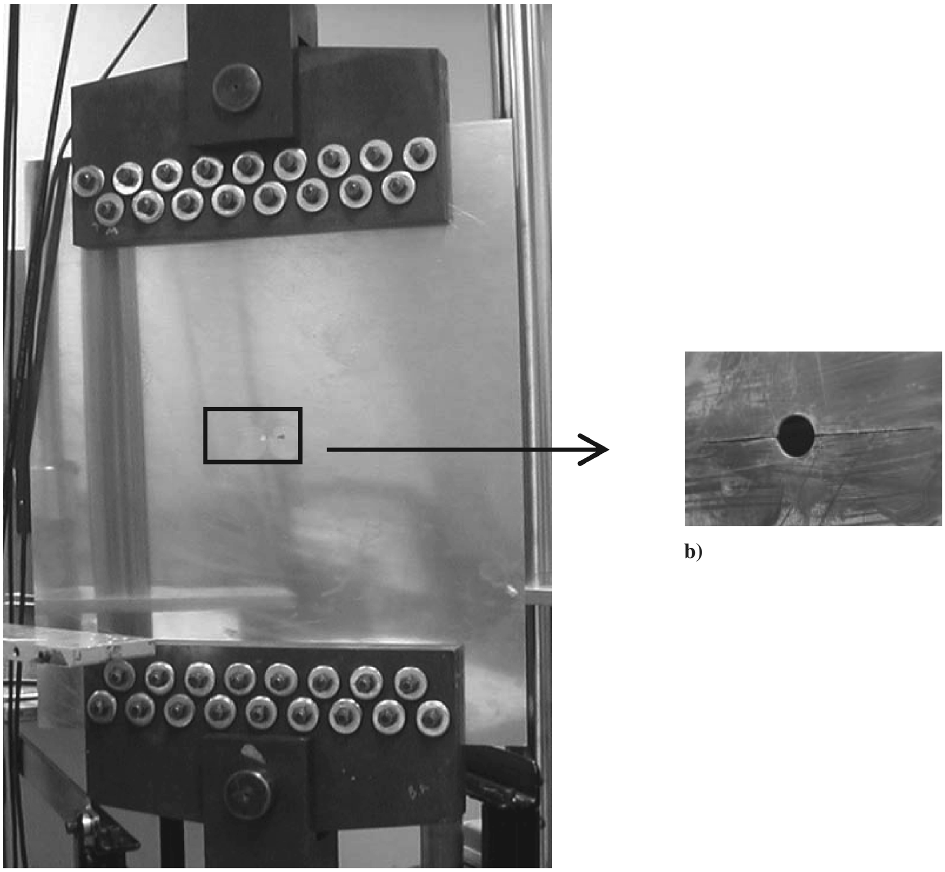
a)
b)

Fig. 9 Experimental setup for fatigue testing without PWAS: a) specimen no. 1 loaded in the MTS 810 testing machine, b) notched hole serving as initial crack.

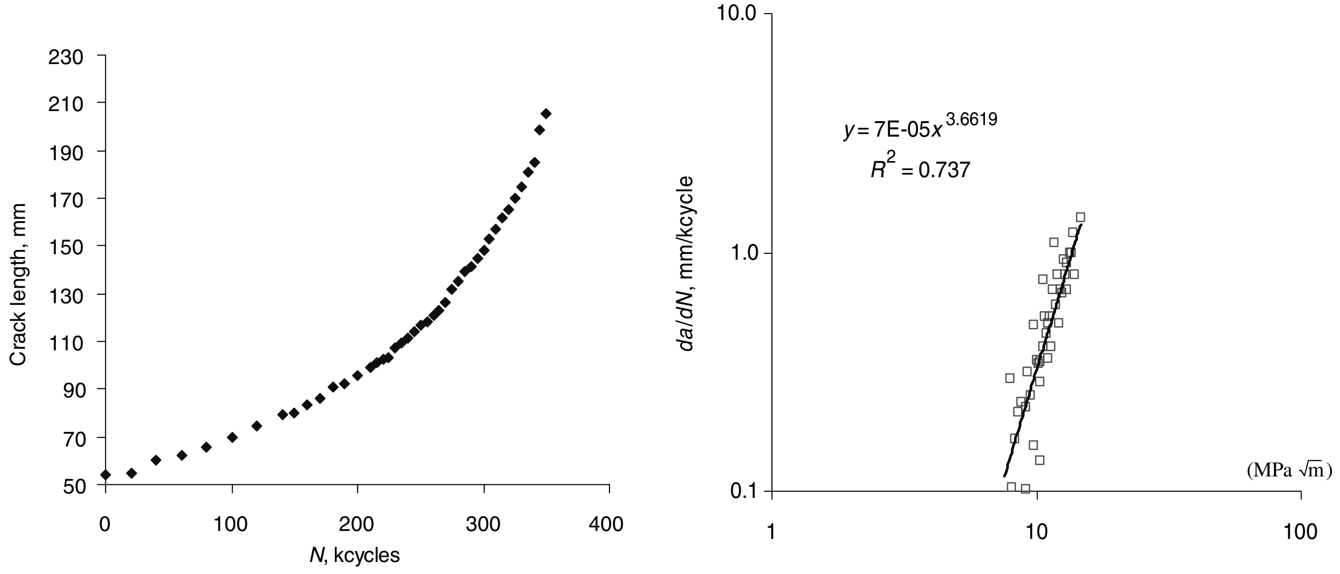

a) b)

Fig. 10 Crack-growth history for specimen no. 1: a) actual crack-length growth vs loading cycles, b) Paris law fit curve for the EUSR measurements, representing crack-growth rate vs stress-intensity factors.

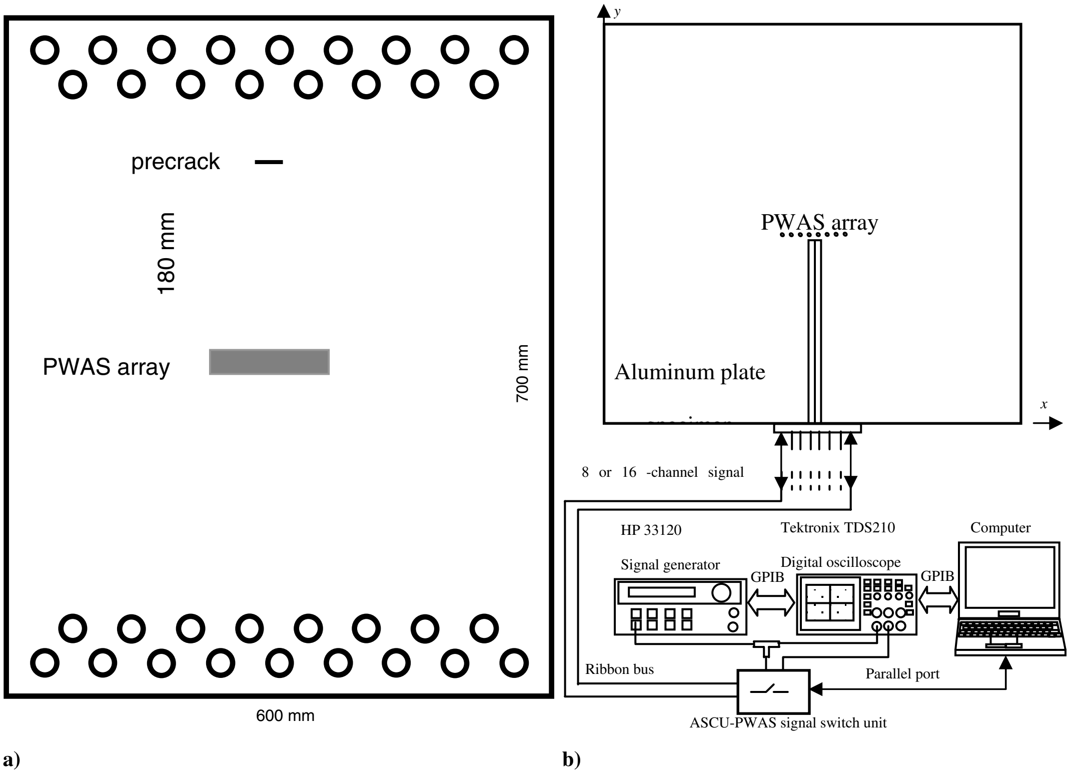

a) b)

Fig. 11 Schematic of experimental setup for fatigue testing with PWAS: a) specimen no. 2 showing installation of PWAS array and location of precrack, b) instrumentation schematics.

2) Determine if PWAS would survive the fatigue cycling without disbonding from the specimen.

The first issue was crucial to the experimental premises. The adverse factors to be clarified were connected with the relative weakness of the Lamb waves generated by our experimental setup in comparison with the rather large noise signals generated by the vibration of the specimen in the loading frame during the cyclic loading. Our initial tests proved that this was indeed so: the Lamb-wave signal was buried in the vibration noise. Because the frequency of the noise (approximately 10–100 Hz) is mostly outside the frequency band of the Lamb-wave signals (300–400 kHz), we were able to use a simple high-pass resistor-capacitor (RC) filter in the electrical systems (as seen in Fig. 13) to reject the noise while maintaining the useful Lamb-wave signal. The RC filter is placed between the PWAS transducer and ASCU system before the signal is recorded and the cutoff frequency was set at 1 kHz. A comparison of the signal before and after applying the filter is given in Fig. 14. Figure 14 gives the graph of pulse-echo between PWAS 0 (most right) and PWAS 5 in the phased array during fatigue cycling. Note that the reflection from the crack is clearly distinguishable after a filter was added to the data collection. This has proven the feasibility of online data collection when the specimen is under fatigue test.

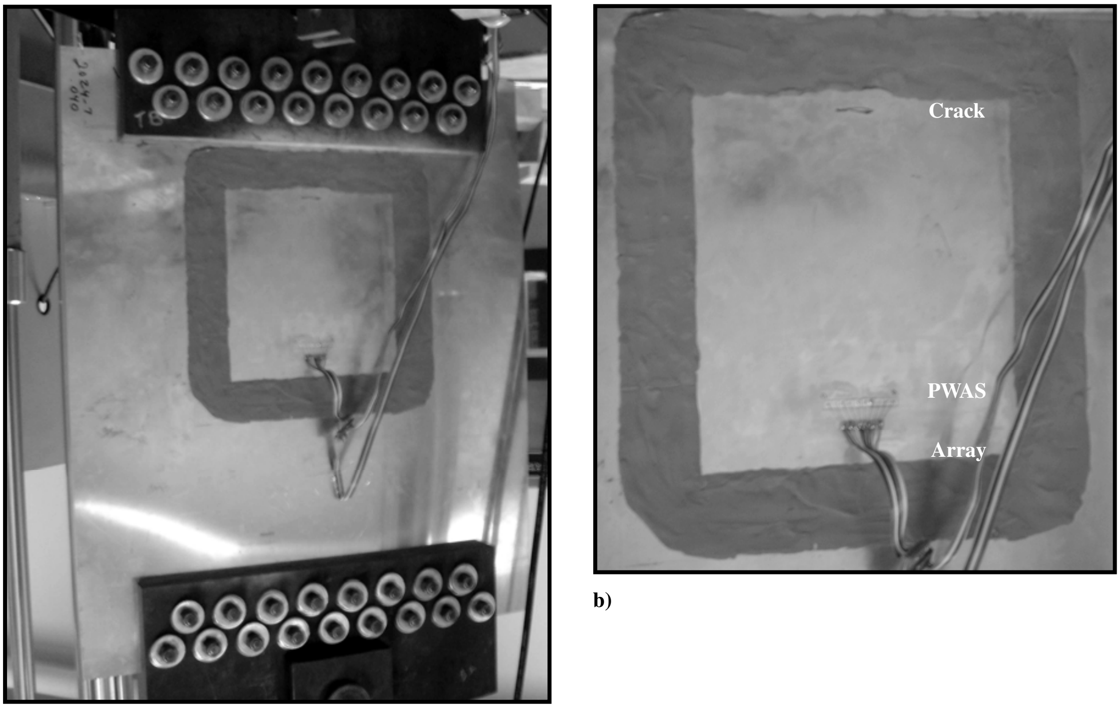

a) b)

Fig. 12 Experimental setup for fatigue testing with PWAS: a) overall picture showing specimen no. 2, b) detail showing PWAS array, crack, and clay dam.

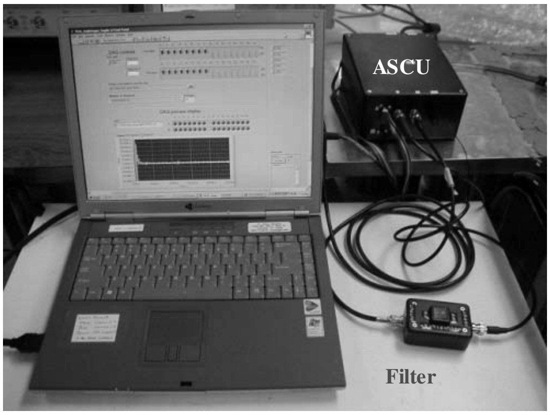

Fig. 13 The high-pass RC filter is placed between PWAS transducer and ASCU system.

The second concern addressed during the fatigue testing with PWAS was that of PWAS survivability. In previous work [27], we proved that a PWAS can remain bonded to dog bone fatigue specimens with stress concentrations up to specimen failure if proper bonding methods were used. Survival beyond 12 Mcycles was observed [27]. In the present work, we used the same adhesive, surface preparation, and curing procedure as in [27].

To verify the PWAS survival capabilities in the presence of fatigue loading, we selected the cyclic loading such that insignificant crack growth would occur. The selected loading was with $F_{\max} = 17{,}800$ N (4000 lbf) and $F_{\min} = 1780$ N (400 lbf), i.e., $R = 0.1$. Because the precrack size was $2a = 25$ mm, the corresponding stress-intensity factor range was $\Delta K \cong 5.8\ \mathrm{MPa}\sqrt{\mathrm{m}}$. The PWAS readings were taken as follows. First, a baseline set of signals was taken. Then, the specimen was loaded into the tensile machine, and a second baseline was taken with the specimen under static load. Subsequently, the specimen was fatigued for 150 kcycles with readings of crack size being taken every 10 kcycles. The resulting crack-size readings are shown in the first part of Fig. 15. It is noticed

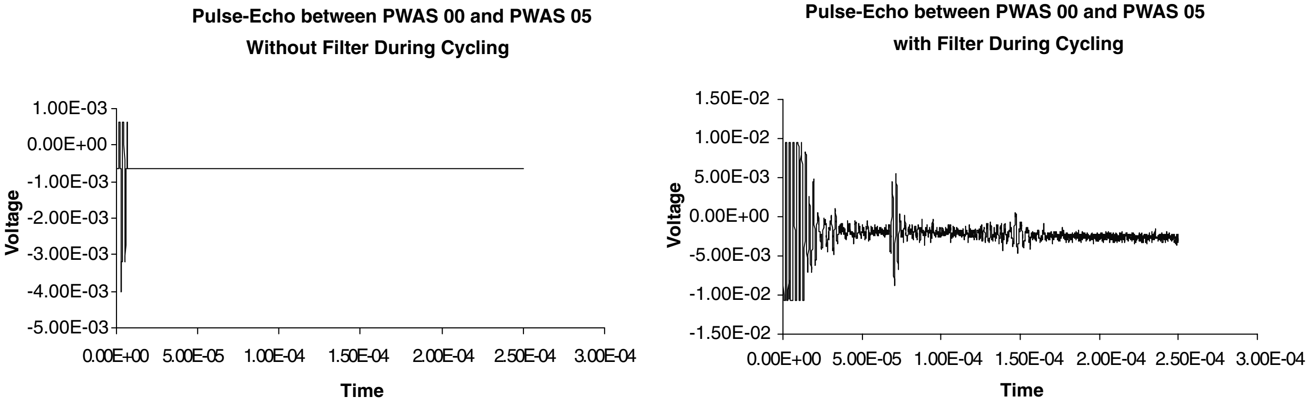

a) b)

Fig. 14 Effect of high-pass filtering on PWAS signal collection: a) no Lamb-wave signals can be observed, b) Lamb wave reflected from the crack can be easily identified.

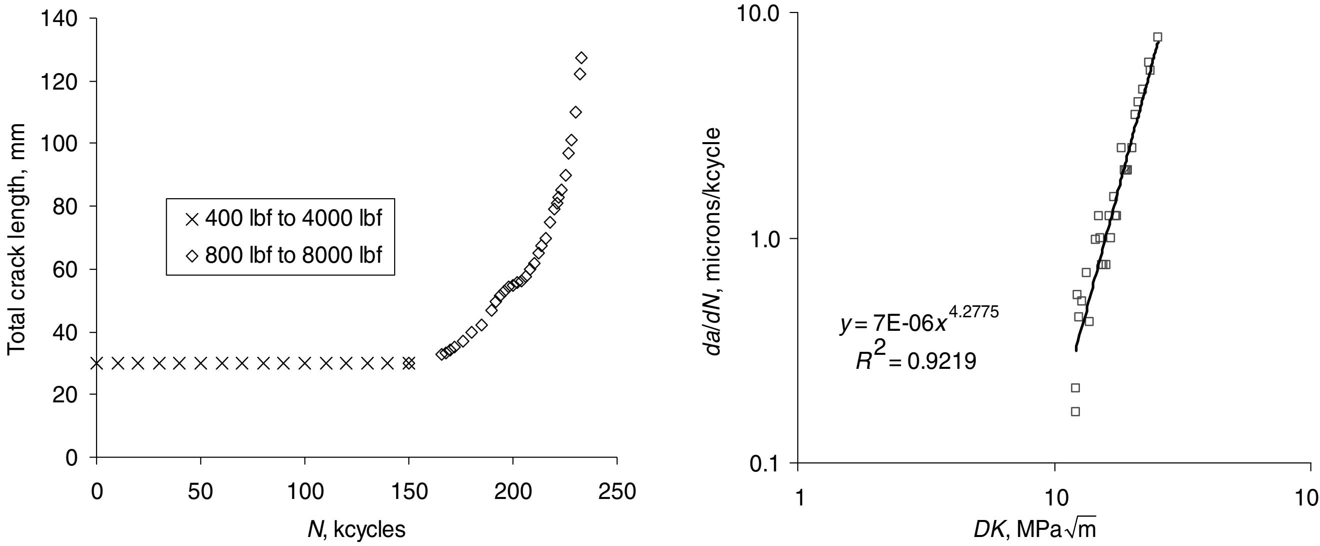

Fig. 15 Crack-growth history for specimen no. 2 instrumented with a PWAS phased array: a) actual crack-length growth vs loading cycles, b) Paris law fit curve for EUSR measurements, representing crack-growth rate vs stress-intensity factors.

from Fig. 15 that during this part of the experiment, no observable crack propagation was produced. By not propagating the crack, a comparison could be made between the baseline scans and the scans made during and after fatigue cycling. No visual discernible difference could be observed in the EUSR imaging. Hence it was concluded that the adhesion method was satisfactory and that no PWAS disbonding occurred during tests.

2. Part 2: In Situ Crack-Growth Detection with PWAS Phased-Arrays During Cyclic Loading

The purpose of Part 2 was to determine if PWAS phased array and the EUSR could detect and quantify the growth of the crack during fatigue loading. To achieve this, we continued the testing of specimen no. 2, but increased the load applied to $F_{\max} = 35,600$ N (8000 lbf) and $F_{\min} = 3560$ N (800 lbf), i.e., $R = 0.1$, again. Crack-size readings were taken at approximately every 2 kcycles. Under these conditions, the crack grew rapidly from 25 to 143 mm over 85 kcycles duration (Fig. 15). The total duration of the fatigue testing was 235 kcycles, of which 150 kcycles at low-load values without crack growth and 85 kcycles at high-load value with crack growth.

Recordings of the PWAS phased-array ultrasonic signals were taken at selected intervals during this crack-growth process. Every reading was taken with two loading conditions: 1) under dynamic conditions, i.e., with the testing machine operating under cyclic loading; and 2) under static conditions, i.e., with the testing machine held at the mean load. As the crack-growth became more rapid, the interval between two consecutive recordings also shortened. Imaging of the crack-growth as resulting from the ultrasonic Lamb-wave phased-array interrogation was performed by the EUSR algorithm. A digital camera optical photograph of the actual crack was also taken, in parallel with the EUSR imaging.

The crack-growth results shown in Fig. 15 indicate that the crack-growth behavior resembles Paris' law. It is significant to note that the crack growth started to accelerate after 220 kcycles, which is consistent with Paris' law. At the end of the experiment, the crack has grown from the initial length of 25 mm to a final length of 143 mm. The corresponding stress-intensity factors were $\Delta K_{\text{initial}} \cong 11.6\ \text{MPa}\sqrt{\text{m}}$ and $\Delta K_{\text{final}} \cong 25.3\ \text{MPa}\sqrt{\text{m}}$.

The EUSR algorithm software tool processes the measured PWAS phased-array data at each cycle and produces an image of the scanning results. The EUSR image was then used to obtain an estimation of the crack size. Figure 16a shows the EUSR front panel. The threshold value, the values δ, and θ of the "dial angles" were controlled from the panel (Fig. 16b). First, an approximate position of the crack edge is obtained with the azimuth dial. If the azimuth dial is turned to an angle where the synthetic beam finds a target and gets a

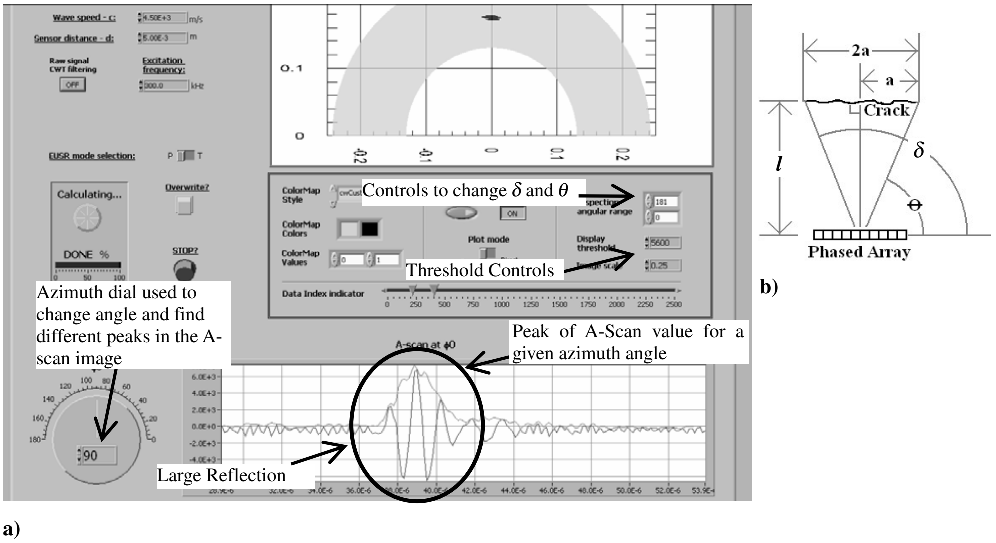

Controls to change δ and θ

Threshold Controls

Azimuth dial used to change angle and find different peaks in the A-scan image

Peak of A-Scan value for a given azimuth angle

Large Reflection

Fig. 16 Determination of crack size from the GUI of the PWAS EUSR program: a) annotated screen capture showing angles and threshold controls of EUSR GUI, b) schematic indicating the θ and δ angles in relation to crack length 2a and distance to target.

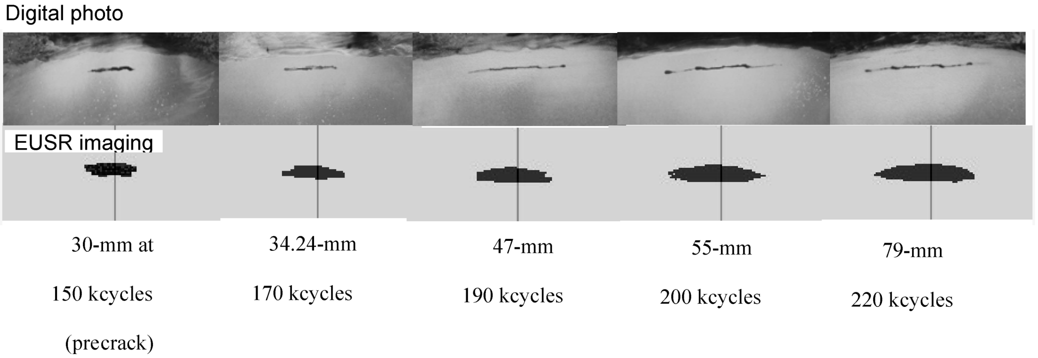

Fig. 17 Comparison between images taken optically and scanned images using EUSR.

reflection, then the A-scan image will show a reflection echo as illustrated in Fig. 16a. After a threshold value was chosen, the θ and δ angles were adjusted such that their rays touched the left and right tips, respectively, of the crack image reproduced in the EUSR graphical user interface (GUI). Figure 17 shows a progression of cracks sizes, as they developed in specimen no. 2 during the fatigue testing, compared with the pictures obtained from a digital camera (note that photos have been adjusted for illustration). The upper row of images contains the optical photos taken with a digital camera. The lower row of images contains the EUSR images of the crack obtained with the PWAS phased-array method. It is apparent that the two rows of the image show good correspondence with respect to crack length vs cycle count.

The length of the crack thus estimated using the EUSR GUI can be easily found using the geometry shown in Fig. 16b, i.e.,

$$2a_{\mathrm{EUSR}} = 2l\tan\left(\frac{\delta - \theta}{2}\right) \tag{12}$$

In our experiment, the distance between the array and the crack was $l = 180$ mm. Hence the EUSR-estimated crack length could be calculated at various numbers of cycles with δ and θ measured by EUSR. The calculated crack sizes are given in Table 2. (Sizes from digital photos are obtained by measuring the crack in the photo.)

During data processing, it was noticed that from 150,000 to 200,000 cycles, the threshold remained the same and the EUSR image of the crack, which grew with the number of cycles, was close to the actual crack size, as measured with optical means. From the calculated results in Table 2, we see that EUSR can correctly measure the crack size with good precision and indicate the growth of crack. Subsequently, we conclude that the EUSR imaging can predict crack growth under fatigue loading.

One thing that has been noticed is that when the crack grew to about 79 mm, the EUSR measurement error rose up to 9.4%, failing to indicate the actual crack growth. Actually, the EUSR image did not grow under the current threshold and the threshold needs to be changed to image the crack with dimensions comparable to the optical measurements. That is to say, in the EUSR crack-length imaging experiment, for up to 200 kcycles, the EUSR measurement is accurate but the crack image did not significantly change as it should above 200,000 cycles. After careful examination, it seems that several aspects concur to upset the crack image calibration as crack length grows beyond a certain value. At this moment, we do not have a full explanation of this effect, but we propose it as a subject of further investigation.

VI. Summary and Conclusions

Active SHM methodology emulates the conventional ultrasonic methods (pitch-catch, pulse-echo, phased arrays, etc.) using guided Lamb waves. Such a methodology will greatly augment the current nondestructive inspection/NDE practice and lead to improved structural state diagnosis, better structural life prognosis, and reduced life-cycle costs. The method for in situ direct measurement of crack growth illustrated in this paper could allow the adjustment of the basic assumptions to improve the crack-growth prediction laws and obtain a better remaining-life estimate of the flight structure. In this paper, we have shown that how piezoelectric-wafer active sensors (PWAS) can be used to monitor crack growth in a thin-wall specimen through a direct ultrasonic imaging technique, the embedded ultrasonics structural radar (EUSR). In the EUSR algorithm, the ultrasonic guided waves (Lamb waves) transmitted and received with PWAS transducers are used in conjunction with the phased-array principle to directly image a thin-plate specimen being fatigued in a testing machine. The imaging was done with a scanning beam of ultrasonic guided waves traveling in the plate. Crack size was then directly measured from the PWAS EUSR image and compared with that obtained from optical photo taken with a digital camera. Comparison and discussion of the experimental results indicated that the crack-growth direct imaging using ultrasonic guided waves and an in situ PWAS phased array compared very well with the photographic images taken with the digital camera. The results confirmed that PWAS transducers technology has a good potential for implementation in active SHM systems.

The direct on-demand ultrasonic imaging of crack growth with in situ PWAS transducers and the EUSR method has proven very effective. Yet certain limitations of the present method were also noticed, due to the distance from the crack to the array, crack orientation with respect to the array [16], and the size of the PWAS phased-array aperture. Further research work should focus on improving the resolution and precision of the PWAS phased-array processing algorithm and synthetic aperture enhancement techniques to refine the crack measurement capabilities.

The current laboratory experiment was conducted on specimens with simple geometry. The next step will be testing the proposed method on realistic aerospace structures toward full industrial implementation. Currently, a clay dam was employed in the

Table 2 Crack sizes measured by EUSR imaging at various loading cycles and comparison with photos taken by digital camera.

Cycles, kcycles	Actual size, mm	Camera measured size, mm	EUSR measured size, mm	Camera error, %	EUSR error, %
150	30	29	31.5	3.3	4.99
170	34.24	32	34.66	6.54	1.24
190	47	45.5	47.39	3.19	0.84
200	55	54	55.09	1.82	0.16
220	79	76	86.43	3.8	9.4

laboratory experiment to eliminate the disturbance resulting from the boundary reflections. Because such a damping dam is impractical in real applications, further research should be invested in the capability of eliminating the boundary reflections through software, i.e., via advanced signal processing. To bring PWAS-based SHM to full fruition, we also envision further research work to be done in several important directions, including 1) the electromechanical coupling between PWAS and the structural Lamb waves, 2) the durability and survivability of the bond between the PWAS and the structure, 3) the in situ fabrication of PWAS transducers directly onto the structure, and 4) integration of the PWAS transducers with the data processing software and wireless communication into small integrated active-sensor units.

Acknowledgments

The financial support of National Science Foundation awards CMS 0408578 and CMS 0528873 and U.S. Air Force Office of Scientific Research grant FA9550-04-0085 are gratefully acknowledged.

References

[1] Giurgiutiu, V., Zagrai, A. N., and Bao, J., "Piezoelectric Wafer Embedded Active Sensors for Aging Aircraft Structural Health Monitoring," *Structural Health Monitoring: An International Journal*, Vol. 1, No. 1, July 2002, pp. 41–61.

[2] Giurgiutiu, V., "New Results in the Use of Piezoelectric Wafer Active Sensors for Structural Health Monitoring," *46th AIAA/ASME/ASCE/AHS/ASC Structures, Structural Dynamics & Materials Conference and 13th AIAA/ASME/AHS Adaptive Structures Conference*, AIAA Paper 2005-2191, 2005.

[3] Shen, B. S., Tracy, M., Roh, Y. S., and Chang, F. K., "Built-In Piezoelectrics for Processing and Health Monitoring of Composite Structures," *AIAA Journal*, Vol. 1310, April 1996, pp. 390–397.

[4] Lin, X., and Yuan, F. G., "Diagnostic Lamb waves in an integrated piezoelectric sensor/actuator plate—Analytical and experimental studies," *42nd AIAA/ASME/ASCE/AHS/ASC Structures, Structural Dynamics, and Materials Conference and Exhibit*, AIAA Paper 2001-1245, 2001.

[5] Kessler, S. S., Spearing, S. M., and Soutis, C., "Damage Detection in Composite Materials Using Lamb Wave Methods," *Smart Materials and Structures*, Vol. 11, No. 2, 2002, pp. 269–278.

[6] Duquenne, L., Moulin, E., Assaad, J., and Delebarre, C., "Transient Modeling of Lamb Wave Generation by Surface-Bonded Piezoelectric Transducers," *European Workshop on Smart Structures in Engineering and Technology, Proceedings of the SPIE*, Vol. 4763, Society of Photo-Optical Instrumentation Engineers, Bellingham, WA, March 2003, pp. 187–193.

[7] Tua, P. S., Quek, S. T., and Wang, Q., "Detection of Cracks in Plates Using Piezo-Actuated Lamb Waves," *Smart Materials and Structures*, Vol. 13, No. 4, 2004, pp. 643–660.

[8] Di Scalea, F. L., Matt, H., and Bartoli, I., "The Response of Rectangular Piezoelectric Sensors to Rayleigh and Lamb Ultrasonic Waves," *Journal of the Acoustical Society of America*, Vol. 121, No. 1, Jan. 2007, pp. 175–187.

[9] Anton, S. R., Park, G., Farrar, C. R., and Inman, D. J., "On Piezoelectric Lamb Wave-Based Structural Health Monitoring Using Instantaneous Baseline Measurements," *Proceedings of SPIE Health Monitoring of Structural and Biological Systems*, Vol. 6532, Society of Photo-Optical Instrumentation Engineers, Bellingham, WA, May 2007, pp. 65320B.

[10] Giurgiutiu, V., and Lyshevski, S. E., *Micro Mechatronics: Modeling, Analysis, and Design with MATLAB*, CRC Press, Boca Raton, FL, ISBN 084931593X, 2004.

[11] Raghavan, A., and Cesnik C. E. S., "Modeling of Piezoelectric-Based Lamb-Wave Generation and Sensing for Structural Health Monitoring," *Proceedings of SPIE, Smart Structures and Materials: Sensors and Smart Structures Technologies for Civil, Mechanical, and Aerospace Systems*, Vol. 5391, Society of Photo-Optical Instrumentation Engineers, Bellingham, WA, July 2004, 419–430.

[12] Bottai, G., and Giurgiutiu, V., "Simulation of the Lamb Wave Interaction Between Piezoelectric Wafer Active Sensors and Host Structure," *Proceedings of SPIE, Sensors and Smart Structures Technologies for Civil, Mechanical, and Aerospace Systems*, Vol. 5765, Society of Photo-Optical Instrumentation Engineers, Bellingham, WA, May 2005, pp. 259–270.

[13] Giurgiutiu, V., Bao, J., and Zhao, W., "Piezoelectric-Wafer Active-Sensor Embedded Ultrasonics in Beams and Plates," *Experimental Mechanics*, Vol. 43, No. 4, Dec. 2003, pp. 428–449.

[14] Giurgiutiu, V., Yu, L., and Thomas, D., "Embedded Ultrasonic Structural Radar with Piezoelectric Wafer Active Sensors for Damage Detection in Cylindrical Shell Structures," *45th AIAA/ASME/ASCE/AHS/ASC Structures, Structural Dynamics & Materials Conference and 12th AIAA/ASME/AHS Adaptive Structures Forum*, AIAA Paper 2004-1983, 2004.

[15] Giurgiutiu, V., Bao, J., and Zagrai, A. N., "Structural Health Monitoring System Utilizing Guided Lamb Waves Embedded Ultrasonic Structural Radar," U.S. Patent No. 6,996,480, 7 Feb. 2006.

[16] Yu, L., and Giurgiutiu, V., "Using Phased Array Technology and Embedded Ultrasonic Structural Radar for Active Structural Health Monitoring and Nondestructive Evaluation," *Proceedings of the ASME IMECE Congress*, International Mechanical Engineering Congress and Exposition Paper 2005-80227, 2005.

[17] Liu, W., and Giurgiutiu, V., "Signal Acquisition/Conditioning for Automated Data Collection During Structural Health Monitoring with Piezoelectric Wafer Active Sensors," *Proceedings of the 5th International Workshop on Structural Health Monitoring*, DEStech Publications, Lancaster, PA, Sept. 2005, pp. 606–618.

[18] Yu, L., and Giurgiutiu, V., "Multi-Damage Detection with Embedded Ultrasonic Structural Radar Algorithm Using Piezoelectric Wafer Active Sensors Through Advanced Signal Processing," *Proceedings of SPIE, Health Monitoring and Smart Nondestructive Evaluation of Structural and Biological Systems 4*, Vol. 5768, Society of Photo-Optical Instrumentation Engineers, Bellingham, WA, May 2005, pp. 406–417.

[19] Clark, W. G., "Fracture Mechanics in Fatigue," *Experimental Mechanics*, Vol. 11, No. 9, Sept. 1971, pp. 421–428.

[20] Paris, P. C., and Erdogan, F., "A Critical Analysis of Crack Propagation Laws," *Journal of Basic Engineering*, Vol. 85, No. 4, 1963, pp. 528–534.

[21] Bucci, R. I., Nordmark, G., and Startke, E. A., *Selecting Aluminum Alloys to Resist Failure by Fracture Mechanisms in Fatigue and Fracture, ASM Handbook*, (edited by) Lampman, S. R., ASM International, Materials Park, OH, Vol. 19, pp. 44073–0002.

[22] Barsom, J. M., "Effect of Cyclic Stress from on Corrosive Fatigue Crack Propagation Below KISCC in a High Yield Strength Steel," *Corrosion Fatigue: Chemistry, Mechanics, and Microstructure*, National Association of Corrosion Engineers, Houston, TX, Jan. 1972, pp. 424–436.

[23] Hartman, A., and Schijve, J., "The Effects of Environment and Load Frequency on the Crack Propagation Law for Macro Fatigue Crack Growth in Aluminum Alloys," *Engineering Fracture Mechanics*, Vol. 1, No. 4, April 1970, pp. 615–631.

[24] McMillan, J. L., and Pelloux, R. M. N., "Fatigue Crack Propagation Under Program and Random Loads," American Society for Testing and Materials STP-415, 1967, p. 505.

[25] Shingley, J. E., and Mischke, C. R., *Mechanical Engineering Design*, 6th ed., McGraw–Hill, New York, 2001.

[26] Bruhn, E. F., *Analysis and Design of Flight Vehicle Structures*, Jacobs Publishing, Phoenix, AZ, 1973.

[27] Doane, J., and Giurgiutiu, V., "An Initial Investigation of the Large Strain and Fatigue Loading Behavior of Piezoelectric Wafer Active Sensors," *Proceedings of SPIE, Sensors and Smart Structures Technologies for Civil, Mechanical, and Aerospace Systems*, Vol. 5765, Society of Photo-Optical Instrumentation Engineers, Bellingham, WA, May 2005, pp. 1148–1159.

A. Palazotto
Associate Editor